S-MRUT: Sectored-Multi Ring Ultrasonic Transducer for Selective Powering of Brain Implants

Seyedsina Hosseini, *Student Member, IEEE,* Kjeld Laursen, *Student Member, IEEE,* Amin Rashidi, *Student Member, IEEE,* Tanmay Mondal, *Student Member, IEEE,* Brian Corbett, and Farshad Moradi, *Senior Member, IEEE*

***Abstract*—One of the main challenges of the current ultrasonic transducers for powering brain implants is the complexity of focusing ultrasonic waves in various axial and lateral directions. The available transducers usually use electrically controlled phased array for beamforming the ultrasonic waves, which increases the complexity of the system even further. In this paper, we propose a straightforward solution for selective powering of brain implants to remove the complexity of conventional phased arrays. Our approach features a Sectored-Multi Ring Ultrasonic Transducer (S-MRUT) on a single piezoelectric sheet, specifically designed for powering implantable devices for optogenetics in freely moving animals. The proposed uni-directional S-MRUT is capable of focusing the ultrasonic waves on brain implants located at different depths and regions of the brain. The S-MRUT is designed based on Fresnel Zone Plate (FZP) theory, simulated in COMSOL, and fabricated with microfabrication process. The acoustic profile of the seven different configurations of the S-MRUT were measured using a hydrophone with the total number of 7436 grid points. The measurements show the ability of the proposed S-MRUT to sweep the focus point of the acoustic waves in the axial direction in depths of $1-3mm$, which is suitable for powering implants in the striatum of the mouse. Furthermore, the proposed S-MRUT demonstrates a steering area with the average radius of $0.862mm$, and $0.678mm$ in experiments, and simulations, respectively. The S-MRUT is designed with the size of $3.8 \times 3.8 \times 0.5mm^3$ and the weight of $0.054gr$, showing that it is compact and light enough to be worn by a mouse. Finally, the S-MRUT was tested in our measurement setup, where it successfully transfers sufficient power to a $2.8mm^3$ optogentic stimulator to turn on a microLED on the stimulator.**

***Index Terms*—Acoustic transducer, Brain implant, Optogenetics, Uni-directional transducer**

I. Introduction

HYBRID brain computer interfaces are entering a new era with the recent advances in miniaturization to develop micro-scale implants interfacing the human brain as anticipated by [1] in 2001. The main motivation behind such implants is diagnosis and monitoring of chronic brain disorders such as Parkinson's Disease (PD), depression, and Alzheimer, which are among the most noticeable disorders, of which around 9 million people will suffer from PD by 2030 in the world [2]. Therefore, any pace in this multi-disciplinary field can have a huge impact on the everyday life of millions of people.

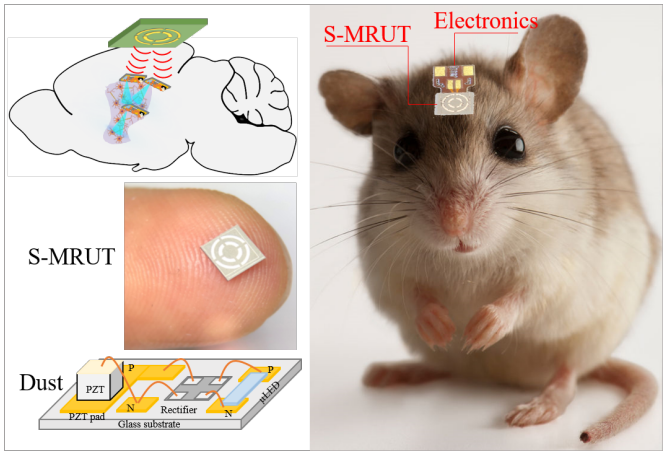

Fig. 1. Conceptual illustration of the S-MRUT on the skull of the mouse for powering the dusts inside striatum.

Nowadays, the only drug to control PD is Levodopa, which alleviates the major motor symptoms [3]. In case of no response to the drug, another emerging approach is deep brain stimulation (DBS) [4]. DBS offers great potential in terms of effective therapeutic durability and treatment of motor impairment. Either of the two methods come with drawbacks such as long-term side effects. Furthermore, deeply penetrating electrodes of DBS systems causes unnecessary tissue damage, and electrical stimulation used for neuromodulation in these systems affects other unnecessary parts of the brain due to low specificity [5]. Recently, optogenetics has found attention from researchers as a method to manipulate genetically modified light-sensitive neurons with optical pulses. Optogenetics offers a high spatiotemporal resolution with cell type specific stimulation [6], [7].

To enable deep optical neuromodulation, fully implantable battery-less and remotely controlled optogenetic devices are among the promising multi-disciplinary research fields to address the challenges of DBS systems [8]. Radio-Frequency (RF) [9], inductive [10], and recently ultrasonic [11], [12] links are among the popular approaches for powering brain implants. Ultrasonic powering outperforms the RF approach for sub-mm sized implants due to its smaller wavelength, less attenuation through brain tissue as well as $72X$ higher Food and Drug Adminstration (FDA)-approved input power

S. Hosseini, K. Laursen, A. Rashidi, and F. Moradi are with the Integrated Circuits and Electronics Laboratory (ICE-Lab) Department of Engineering, Aarhus University, 8200 Aarhus N, Aarhus, Denmark (e-mail:hosseini@eng.au.dk; Moradi@eng.au.dk) T. Mondal and B. Corbett are with the III-V materials and devices group at Tyndall National Institute, University College Cork, Ireland.

Manuscript received

exposed to the body [13], [14]. Therefore, recently, researchers have been developing brain implants that are equipped with a piezoelectric receiver (e.g. Lead zirconate titanate (PZT)) for harvesting energy from an external source [15]–[17]. PZT has been used for implementing miniaturized ultrasonically powered devices (hereafter called dusts) for brain stimulation [11], [16]–[18]. This is important for such devices to be in dust-size to reduce tissue damage in the brain. The conceptual illustration of the system is shown in Fig. 1, where a novel compact and light-weight Sectored-Multi Ring Ultrasonic Transducer (S-MRUT), proposed in this paper can be used for powering such the dusts. We have recently developed a miniaturized dust, which includes $500\mu m \times 500\mu m \times 500\mu m$ PZT-4 cube with $300\mu m \times 130\mu m$ light emitting diode (μLED) [19] and $300\mu m \times 300\mu m$ electronic chip on a $3mm \times 1.5mm$ substrate [16].

In general, commercially available acoustic transducers and MEMS-based ultrasonic transducers have been used in literature for acoustic powering of implants [20]. Commercial devices are bulky and heavy that makes them inappropriate for freely moving animals [21]. MEMS-based ultrasonic transducers i.e. piezoelectric micromachined ultrasonic transducer (pMUT) and capacitive micromachined ultrasonic transducer (cMUT) have shown promising results for various applications such as imaging [22], haptic [23], and neuromodulation [24]. Although these devices come in various shapes, resonance frequencies, and acoustic intensities [25], [26], smaller transducers with higher intensity are desirable for acoustic powering of implants in freely moving animals [27], [28]. Furthermore, the need for selective powering of dusts, placed in different locations in the brain, are addressed by beamforming [29] or physical lenses [30] in the literature, which increases the complexity of the system, considerably. As a completely different approach, we have proposed an MRUT in [31] for focusing the acoustic waves in the axial direction in front of the transducer. Here, we propose a novel transducer enabling the sweeping of ultrasonic waves in both lateral and axial directions.

II. Theory

To focus light without lens, Fresnel Zone Plate (FZP) theory has been used in literature [32], which contains concentric rings to diffract waves when they pass through the rings. These waves will constructively interfere with each other, if the distance between the rings are designed accurately. To use this theory for ultrasonic link and our application, two rings with path lengths R_1, R_2, R_3, R_4 and radii r_1, r_3, r_5, r_7 are considered as illustrated in Fig. 2. For a full circle, in order to focus the waves at one point, the path length difference between the sources should follow this equation [33]:

$$R_{i+2} - R_i = m\lambda \tag{1}$$

where i and m are positive integers, and λ is the wavelength in medium. However, for a ring-shape configuration, since the electrodes have a width, the edges of each electrode should fulfill the following criteria to minimize the destructive interference of the waves at the focal point:

$$R_{i+1} - R_i = \lambda/2 \tag{2}$$

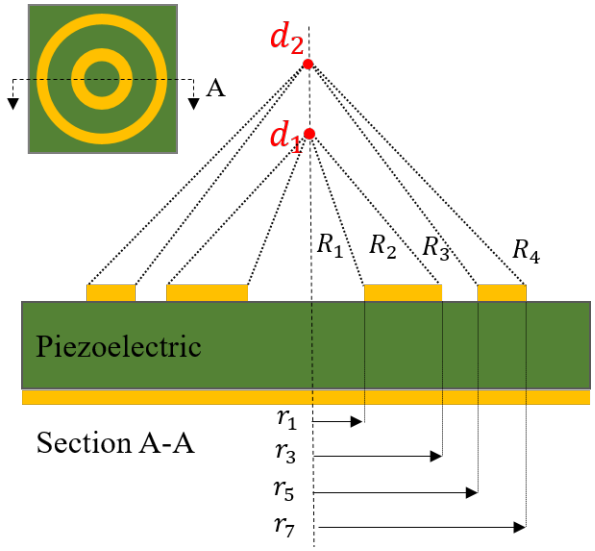

Fig. 2. Cross-sectional view of the fresnel zone plate with multi symmetrical rings as an acoustic transducer.

The proposed S-MRUT is composed of two rings each of them consists of four equal-length sectors. Let us consider two different focal points d_1 and d_2 for inner and outer rings, respectively. Then, in order to satisfy the conditions in equations (1) and (2), the radius of electrodes can be calculated using the following equation:

$$r_n = \sqrt{\frac{\alpha\lambda}{2}(d + \frac{\alpha\lambda}{8})} \tag{3}$$

where d is the focal point, $n = 1, 3, 5, ...$, $\alpha = n + 1 + 2\delta$, and δ is the offset value that relates to the discrepancies between the calculated and measured focal point due to the fabrication process with values of $-1 < \delta \leq 0$. The best focusing can be achieved with $\delta = 0$. Therefore, one can design the electrodes to focus the acoustic energy on the axis along the transducer. However, for only one sector of each ring electrode as the acoustic source, the superposition of the waves will be off-axis. The reason for the off-axis focal point is the distance g between acoustic sources and thus the resulting time delay because of the distance. In order to explain the reason of the off-axis focal point, let us take two acoustic sources a and b as small fractions of inner and outer rings, respectively, as shown in Fig. 3. Based on the Huygens' Principle [34], small sound sources create V-shaped beams. The superposition of the beams will be either constructive or destructive. If they constructively interfere at point x, there is a time delay Δt because of the distance g. As a consequence, a phase shift ϕ caused by the time delay that can be calculated with the following equation:

$$\phi = 2\pi f \Delta t = \frac{2\pi}{\lambda} g \tag{4}$$

where f is the frequency. For the S-MRUT, the two aforementioned fractions have an equal distance g and if we integrate their effect over one sector of the ring, the off-axis focal point will be achieved.

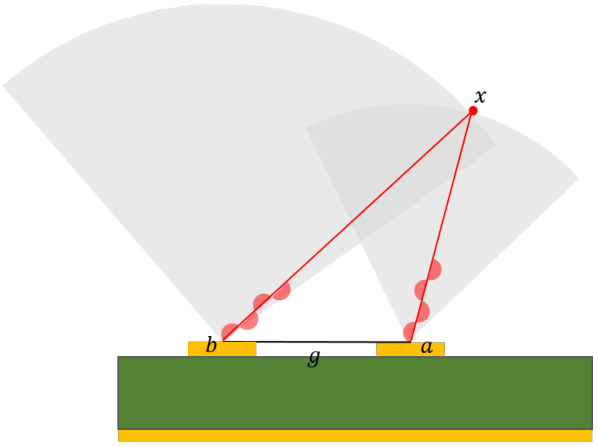

Fig. 3. Cross-sectional view of the emitted waves from two fraction of rings.

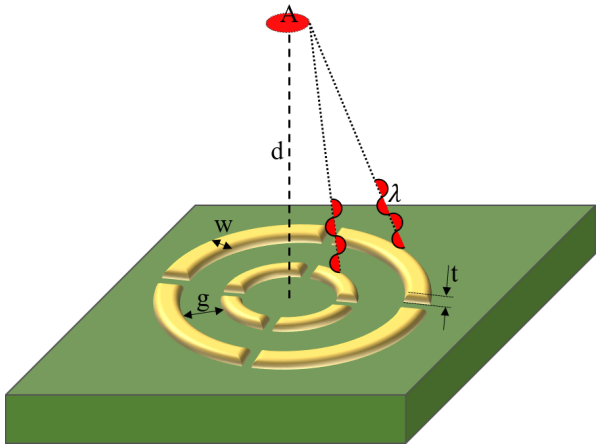

Fig. 4. Design parameters of the S-MRUT.

III. Design and Simulation

A. Design considerations

Main design objectives for designing a transducer for our application can be listed as below:

1) Steering area: To power the dusts in various locations, the transducer should be designed in a way that the maximum acoustic pressure occurs at the desired angle, otherwise the distributed pressure in other directions will reduce the efficiency of the transducer [35]. Therefore, one of the main design objectives, is to maximize the steering area (A) where the maximum pressure takes place, and we can implant the dusts in that area. Since the dusts will be implanted on the surface of striatum of mice, which has a spherical shape with a radius of $\approx 1.5mm$ [36], larger steering area should be targeted for designing the transducer.
2) Ratio of main to side lobe amplitudes: In order to reduce the loss of ultrasonic energy in other directions, the amplitude ratio of the main to side lobe needs to be maximized. In other words, a transducer with a smaller main to side lobe amplitude ratio, gives higher reflections from the tissues located in regions under the side lobes.
3) Main lobe width: For decreasing the attenuation of acoustic energy in brain tissue, the beam width of the transducer should be small, otherwise the sound beam will not be well directed to the target.
4) The focal distance (d) is also important for powering the dusts with maximum acoustic intensity.

To achieve the proper design, available design parameters, as shown in Fig. 4 are the wavelength (λ) in medium, element distance (g), element width (W), electrode thickness (t), and the number of electrodes (N). Among the aforementioned parameters, the distance (g) and width (W) are calculated based on the electrodes' radii and the equation (3) for our desired focal points, as explained in the previous section. Here, we consider a focal distance (d) of $1mm - 3mm$, which is the distance from the skull surface of the mice to the motor cortex and the striatum. In this work, λ depends on the size of the piezoelectric receiver in the implantable dust, which defines the operating frequency. In other words, the resonance frequency of the piezoelectric receiver (i.e. the proper operating frequency for the dust) and consequently the wavelength of ultrasonic waves in the medium depends on the dimensions of the piezoelectric receiver. The electrode thickness is fixed at $10\mu m$ in this work. Finally, the higher number of electrodes (N) is a factor that gives us more selectivity on the off-axis focal point as proposed in this work. However, N is also limited because of the electrical connections on the Printed Circuit Board (PCB) as well as the space constraint on the piezoelectric substrate.

B. COMSOL simulation

Based on the ideas and theories presented in previous sections, the transducer is modeled and simulated in COMSOL 5.4 (COMSOL, Burlington, MA, USA) for characterizing the acoustic pressure and the intensity profiles in the medium as well as finding the steering area by means of parameters. In all simulations, the transducer and the water domain were modeled in 3D, and PZT-4 is selected as the piezoelectric material. The maximum acoustic intensity for the simulations is considered as 7.2 mW/mm^2 based on the maximum FDA-regulations intensity for acoustic waves in human body [13]. To model the sectored ring electrodes on the surface of piezoelectric substrate, shell module is also implemented in the simulations. Then, the pressure acoustics, solid mechanics, and electrostatics in frequency domain were solved as physics of the simulation. Regarding the boundary conditions, as shown in Fig. 5, the S-MRUT is simply supported in solid mechanics module (Fig. 5(a)). In the electrostatics, the sectors of top electrodes are considered as the positive electrodes (Fig. 5(b)) and the bottom surface as the ground electrode (Fig. 5(c)). In the pressure acoustics module, the spherical wave radiation node is selected as the radiation boundary condition to remove the reflections (Fig. 5(d)). For coupling the aforementioned physics, the multiphysics node is added to the model with the sub-nodes of piezoelectric effect and acoustic-structure boundary. The former is responsible for coupling the solid mechanics and electrostatics, and the latter for coupling the pressure acoustics and solid mechanics.

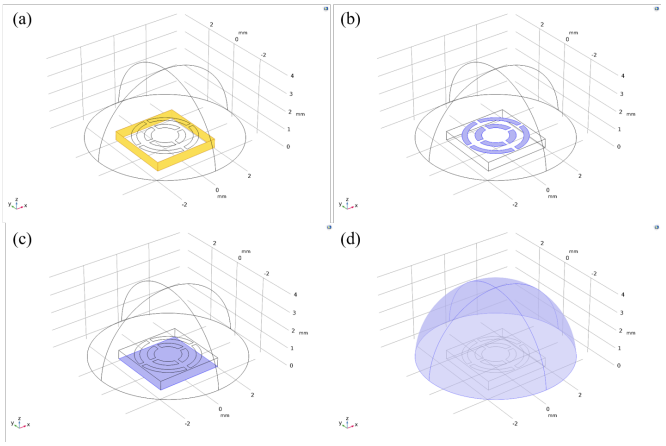

Fig. 5. Boundary conditions for (a) solid mechanics module with simply supported plate, (b) electrostatics with the sectors of top electrods, (c) electrostatics with the ground electrode, and (d) pressure acoustics with the spherical wave radiation.

In our simulations, first, the resonance frequency of each cubic size of piezoelectric for the dust was modeled. As mentioned earlier, the resonance frequency and consequently the wavelength, were selected based on the resonance frequency of the piezoelectric receiver in the dust. Fig. 6 shows the results for different cubic sizes of the piezoelectric receivers. Since the dusts includes a piezoelectric receiver with the dimension of $0.5mm \times 0.5mm \times 0.5mm$, the operating frequency of $2.9MHz$ has been chosen for the S-MRUT. The piezoelectric plate with $0.5mm$ thickness is selected for the S-MRUT, the same as the piezoelectric receiver in the dust. Before doing the simulations on the acoustic profile of the S-MRUT, we need to find the desired mode shape around the selected frequency. Choosing the correct mode shape is one of the important steps in designing the transducer, since each geometry has a specific mode shape with a given profile for the displacement, which relates to the output pressure. The preferable mode shapes are gaussian and piston-like, as they can symmetrically

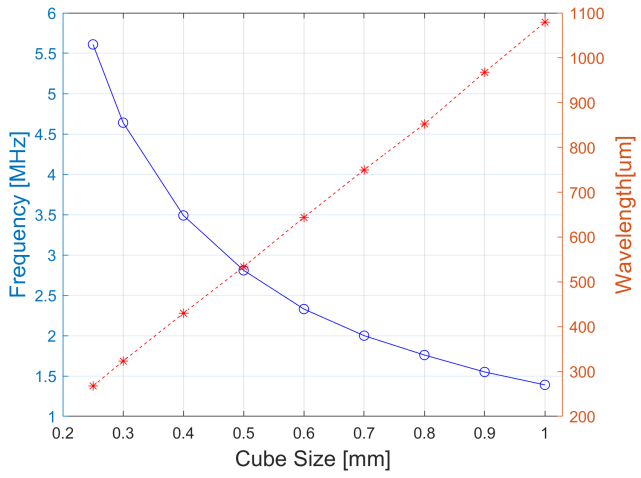

Fig. 6. Simulation of the resonance frequency over the different sizes of piezoelectric receiver in dusts.

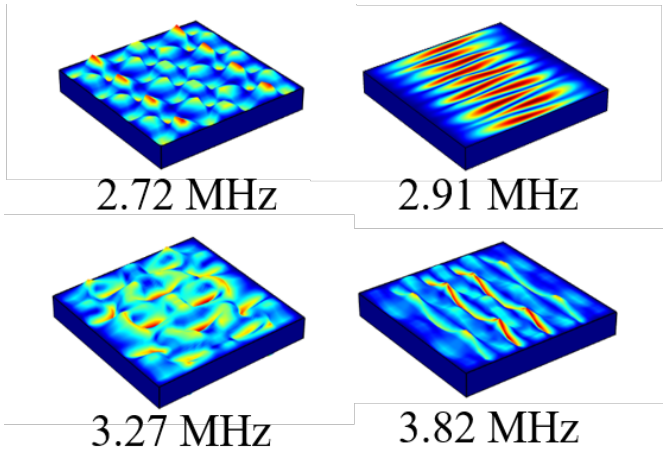

Fig. 7. Simulation of the eigenmodes for the piezoelectric plate. Dark blue color represents the zero displacement and dark red color is for the maximum one.

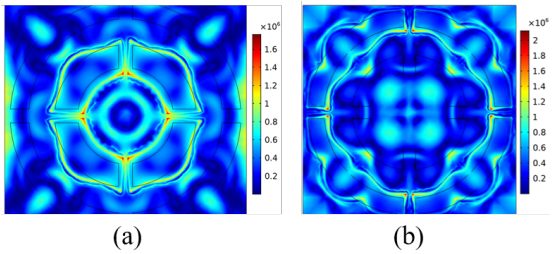

Fig. 8. Simulations of the mechanical stress for (a) inner active electrodes, and (b) outer active electrodes.

vibrate with the maximum displacement around the center. Since these two mode shapes occur in the frequency range of kilohertz in our transducers, they were not selected. In other words, the frequency range of kilohertz is equal to few millimeter wavelength which is not appropriate for us in terms of the desired focal distance. To find the desired mode shape, eigenfrequency simulations were carried out as shown in Fig. 7. As illustrates in the figure, each mode shape includes vibrations in thickness and flexural modes. However, the desired mode shape is the one with higher vibrations in thickness direction. Based on the figure, the mode shape with frequency of $3.27MHz$ has been selected due to the symmetrical vibrations in thickness direction around the center. Based on the size of the piezoelectric receiver in the dust and the mode shape, the frequency was selected. In the next step, the electrodes' rings on top of the piezoelectric plate should be patterned. Since the active area on the piezoelectric plate is the region with electrodes, only the top electrodes should be designed. However, this depends on the mode shape, and the electrodes should be mainly placed on a region with the highest degree of displacement in eigenfrequency simulation. Thus, the electrodes' radii are designed based on the equation (3) with the desired focal distances $(1 - 3mm)$. The electrodes are designed in a way that the inner electrodes have a focal distance at $1mm$, the outer electrodes focus the waves at $2.5mm$, and the whole transducer focuses the waves

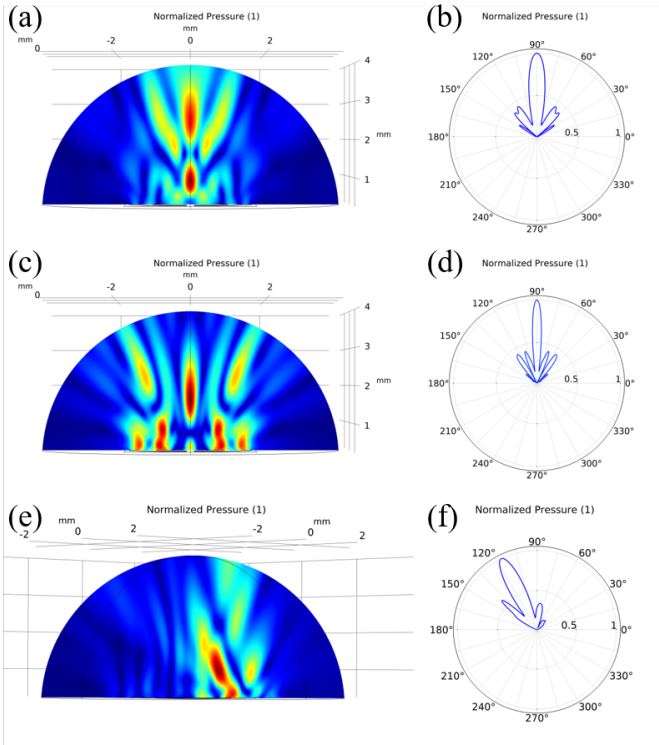

Fig. 9. Simulated normalized acoustic pressure for inner electrodes in (a) and (b), outer electrodes in (c) and (d), and sectored electrodes at the same quarter (e) and (f). In the plane normal to the S-MRUT surface (a),(c), and (e) dark red shows the maximum pressure and dark blue is for the minimum pressure.

at $3mm$. As shown in Fig. 8 (a), when the inner electrodes are active, the maximum mechanical stress occurs around the inner electrodes. However, for the outer active electrodes in (b), the maximum stress and consequently the maximum displacement are around the outer electrodes.

After designing the electrodes with the desired requirements, we measure the steering area, the main lobe width, and the ratio of the main to side lobe amplitude. In Fig. 9, the simulation results for the normalized pressure in a plane normal to the S-MRUT surface, and also the polar plot are shown. Figs. 9 (a) and (b) illustrates the acoustic profile for the inner electrodes, (c) and (d) for the outer electrodes, and (e) and (f) for sectored electrodes at the same quarter. As expected, the inner and outer electrodes direct the waves in the axial direction in front of the S-MRUT, however, sectored electrodes at the same quarter are able to focus the waves $0.678mm$ off-axis. In other words, with the designed electrodes, we can have a steering area of $1.443mm^2$ if only one sector of each ring at the same quarter is driven by an electrical signal. The main lobe width for the sectored electrodes at the same quarter is $0.46mm$, which is larger than the inner electrodes with $0.4mm$ and the outer electrodes with $0.35mm$. The larger main lobe width for the sectored electrodes at the same quarter is attributed to the asymmetrical stimulation of the transducer. The main to side lobe ratio is greater for the inner and outer electrodes when compared to the sectored ones. Increasing the number of electrodes would improve the main to side lobe ratio.

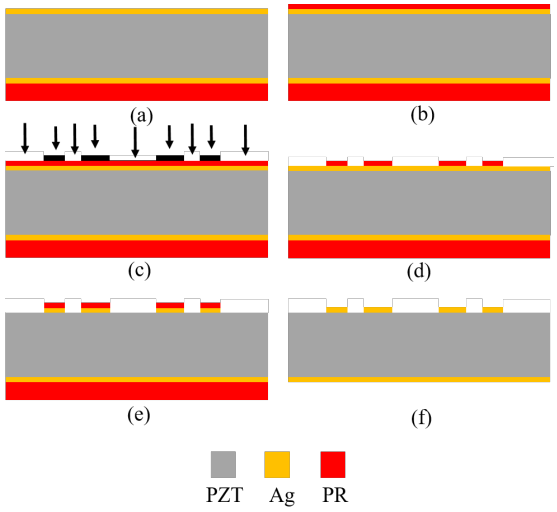

Fig. 10. Fabrication process includes (a) protecting the backside of the substrate with Si wafer, (b) spin coating photoresist on the front side, (c) photo-lithography, (d) developing the photoresist, (e) silver etching, and finally (f) removing the photoresist on both sides.

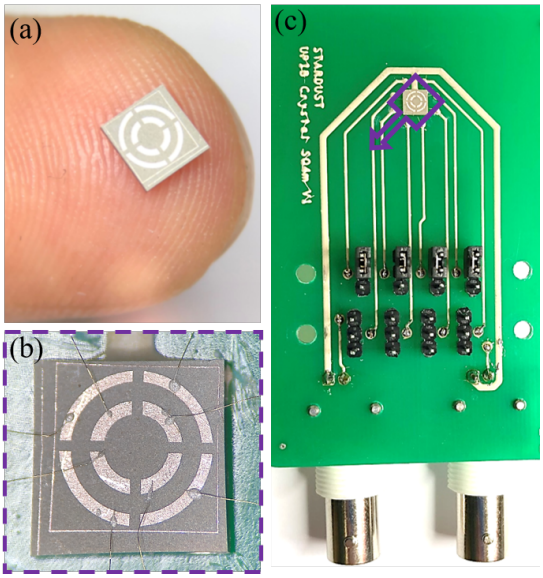

Fig. 11. (a) Size of the S-MRUT compared to the finger. Magnified view of the S-MRUT in (b) on custom-designed PCB in (c).

IV. Experimental Results

A. Fabrication process

For our experiments, we used a PZT-4 (APC International, Mackeyville, PA) plate of $10mm \times 10mm$ with a thickness of $0.5mm$, which is silver coated $10\mu m$ on both sides. The fabrication process is illustrated in Fig. 10. As the first step, a two-step cleaning process of the sample in acetone, followed by isopropyl alcohol in an ultrasonic bath for 5 minutes, is performed. The substrate is then baked for 2 minutes at $120°C$ to remove the water from the surface and enhance the resist adhesion. The backside electrode is covered with a

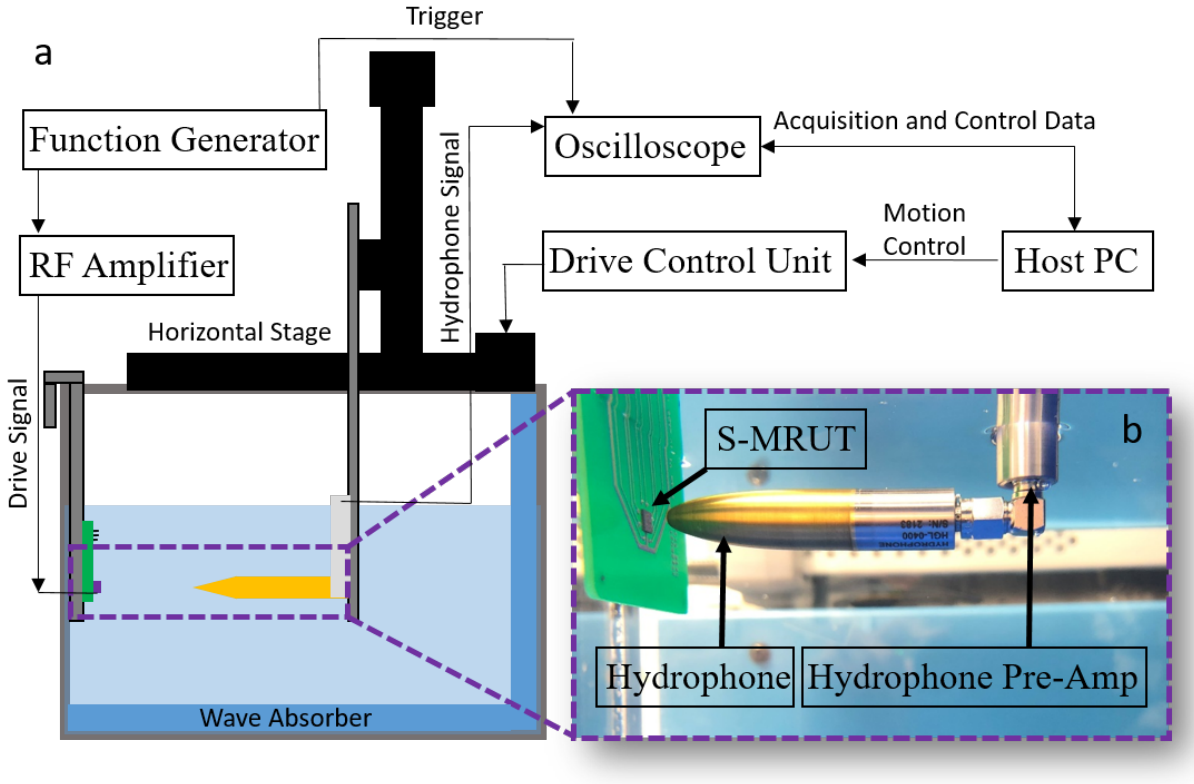

Fig. 12. (a) Diagram of the measurement setup, (b) photograph of the scanning region.

silicon wafer using a drop of photoresist and baking it for 10 minutes at $120°C$. Then, $1.8\mu m$ photoresist $AZ1518$ (Clariant Corp., Somerville, NJ) is spin-coated on the top surface at $4000RPM$, and baked for 3 minutes at $100°C$. To make sectored patterns on the top electrode, photo-lithography is carried out. Then, to improve the chemical stability of the resist mask during the etching process, hard-bake is done for 10 minutes at $145°C$. After cooling down the sample to room temperature, it is etched in a silver etchant. After patterning the top electrodes, the PZT plate is diced with a Disco DAD321 (Disco Corporation, Tokyo, Japan) ($20000RPM$ spindle speed and $1(mm/s)$ feed rate) in the size of $3.8mm \times 3.8mm$ as shown in Fig. 11 (a). Then, for measurement purposes, the fabricated S-MRUT is mounted on a custom-designed PCB using ESL 1901-S polymer silver conductor paste (ESL ElectroScience Europe, Berkshire, UK) and cured at $80°C$ for 30 minutes, thereby connecting the bottom electrode to the PCB. Top electrodes are wire-bonded manually with a $17\mu m$ Au wire to the PCB as shown in Fig. 11 (b). On this PCB, the configuration of the driven sectors is done using some jumpers that can connect each sector to one of the two input BNC connectors, as shown in Fig.11 (c).

B. Acoustic profile measurement

The acoustic profiles of the S-MRUT for different configurations of the electrodes under excitation are measured using the setup shown in Fig. 12. In this setup, an arbitrary signal generator (Agilent Technologies 81160A, Keysight Technologies, Inc., Santa Clara, CA, USA) is used to generate the sinusoidal signal and drive the S-MRUTs' sectors under test. The acoustic intensity at each relative position to the S-MRUT is measured using an HGL-0400 hydrophone followed by an AH-2010 pre-amplifier from Onda Corporation (Sunnyvale, California, USA), which is connected to Rhode & Schwarz RTO 1044 Oscilloscope (Rohde & Schwarz International GmbH, Germany). For plotting the S-MRUT's output acoustic profile over a certain volume of water tank, the hydrophone is moved using a Velmex micro-positioning system (Velmex Inc., Bloomfield, NY) with a resolution of down to $5\mu m$. The micro-positioning system, signal generator, and oscilloscope are all controlled simultaneously and automatically through MATLAB (Mathworks, Inc., Natick, USA) scripts. The obtained data is retrieved directly from the oscilloscope via Ethernet LAN and saved by MATLAB on a connected computer. For all measurements, the hydrophone is initially located in the center position of the S-MRUT with a $1mm$ distance. The initial $1mm$ distance is measured based on the time-of-flight of acoustic wave in water ($1484(m/s)$). Measurements are conducted in de-ionized water in a custom-designed plexiglass water tank equipped with AptFlex F28 (Precision Acoustics, Dorset, UK) wave absorbers to dampen the reflected waves from the tank's walls.

To characterize different configurations of electrodes, our desirable scanned volume in front of the S-MRUT was a cube of $5mm \times 5mm$ in each slice with $5mm$ in depth. The resolution of scanning profile in each slice is $200\mu m$, however

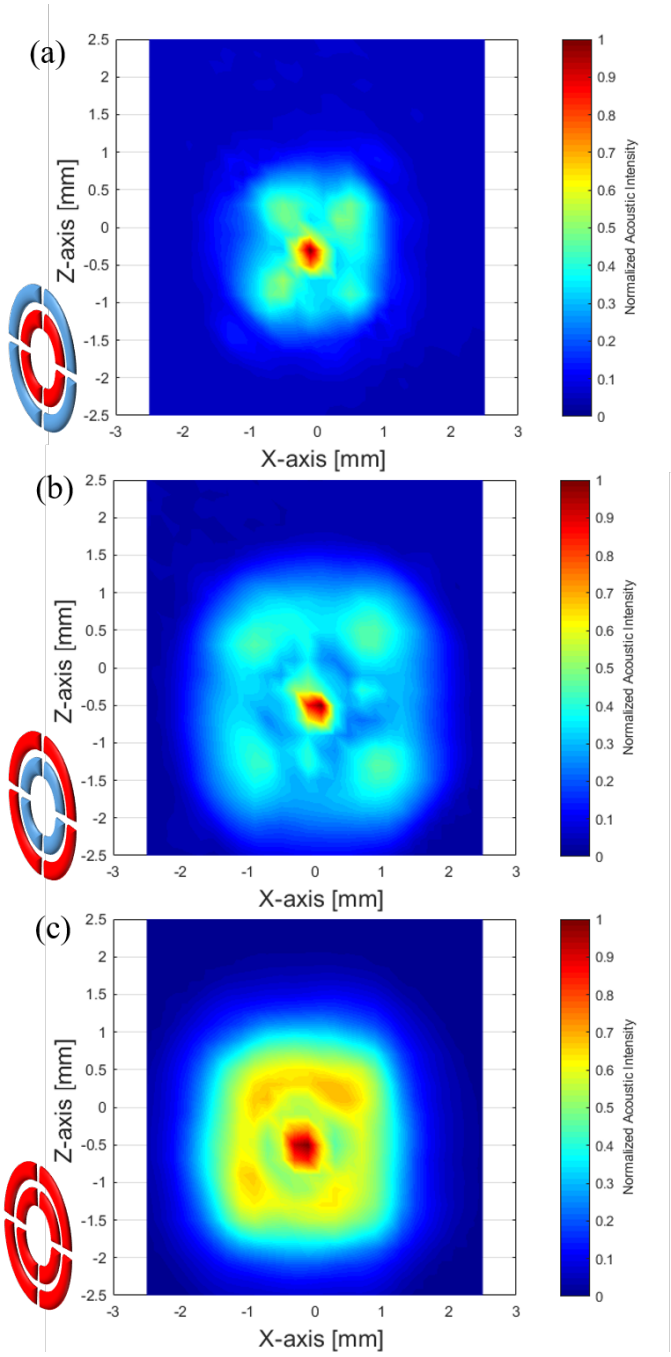

Fig. 13. Acoustic profile measurements of (a) the inner, (b) the outer, and (c) all active electrodes. It should be noted that in the schematic of the S-MRUT near each measurement, red shows the active electrodes and blue is for the inactive ones.

the gap between each slice is $500\mu m$. In all measurements, all sectors are driven by a sinusoidal signal within the frequency range of $2.5-3.5MHz$ with a step of $0.1MHz$ and the amplitude of $5V_{pp}$. It should be noted that in each measurement, in total 7436 grid points are scanned.

The acoustic profile of the inner electrodes is illustrated in Fig.13 (a). The maximum acoustic intensity occurs at $1mm$ distance at $3.5MHz$ on the axial direction along the central axis of the S-MRUT, and it starts to decrease after the focal point. The lateral resolution is quantified by calculating the Full-Width-Half-Maximum (FWHM) which is $550\mu m$.

Fig.13 (b) shows the acoustic profile of the outer electrodes where the maximum acoustic intensity is on the axis along the S-MRUT at $2.5mm$ distance at $3.5MHz$. Because of the larger activated area of the S-MRUT, the acoustic profile is distributed more than the inner electrodes. The FWHM here is $500\mu m$.

Fig.13 (c) shows the acoustic profile of the S-MRUT when all electrodes are driven by the same electrical signal. In this case, the acoustic intensity is distributed with higher amplitude and a wider area in comparison with driving only one of the inner or outer electrodes. The maximum intensity is at $3mm$ on the central axis at the frequency of $3.2MHz$, where the FWHM is $600\mu m$.

Each of the sectored electrodes at the same quarter are driven separately. Fig.14 (a) illustrates the acoustic profile of driving the two sectors at the top left quarter. In this case, the maximum acoustic intensity and FWHM are measured in $700\mu m$ off-axis and $800\mu m$, respectively. In Fig. 14 (b), the two electrodes in the top right quarter are activated, and they have the maximum intensity at $650\mu m$ off-axis and the same FWHM as before. Fig. 14 (c) shows the two electrodes in the bottom left quarter. In this case, the maximum intensity is at $1.1mm$ off-axis with the same FWHM. Fig. 14 (d) shows the two electrodes in the bottom right quarter giving the maximum intensity at $1mm$ off-axis and the same FWHM; however the acoustic profile for this setup is different from the others, and the focal point is at $1mm$. The reason for this discrepancy may come from the variation of the dimension of the electrodes due to the etching variability in fabrication process. The maximum intensity for all of these four cases is occured at $3.5MHz$. Experimental results show that for the sectored electrodes at the same quarter of the S-MRUT, one can focus the acoustic waves off-axis, thereby increasing the steering area for powering the dusts. Furthermore, it should be noted that for these cases, the main lobe width is larger than the inner, outer, and all excited electrodes which is due to the asymmetrical configuration of the transducer.

C. Demonstration and application

To verify the S-MRUT for powering implantable dusts, we immersed the S-MRUT and a dust in a water tank as shown in Fig.15. The dust is glued to the PCB and is located in front of the S-MRUT. The inner electrodes of the S-MRUT are driven by the signal generator with an amplitude of $220mV_{pp}$ and a frequency of $2.935MHz$. The signal is amplified with a $50dB$ RF power amplifier. Then the acoustic intensity is calculated with the following equation:

$$I_{rms} = \frac{V_{pp}^2}{8 \times M_l(f)^2 \times Z_m} \tag{5}$$

where V_{pp} is the peak to peak value of the voltage of the hydrophone, $M_l(f)$ in $(\frac{V}{Pa})$ is the sensitivity of the hydrophone that can be found in the data sheet of the hydrophone ($2.0883\times 10^{-}6(\frac{V}{Pa})$ for the given frequency), and Z_m in $(MRayl)$ is the acoustic impedance of the medium ($1.5MRayl$ for water). Thus, the measured acoustic intensity for our S-MRUT

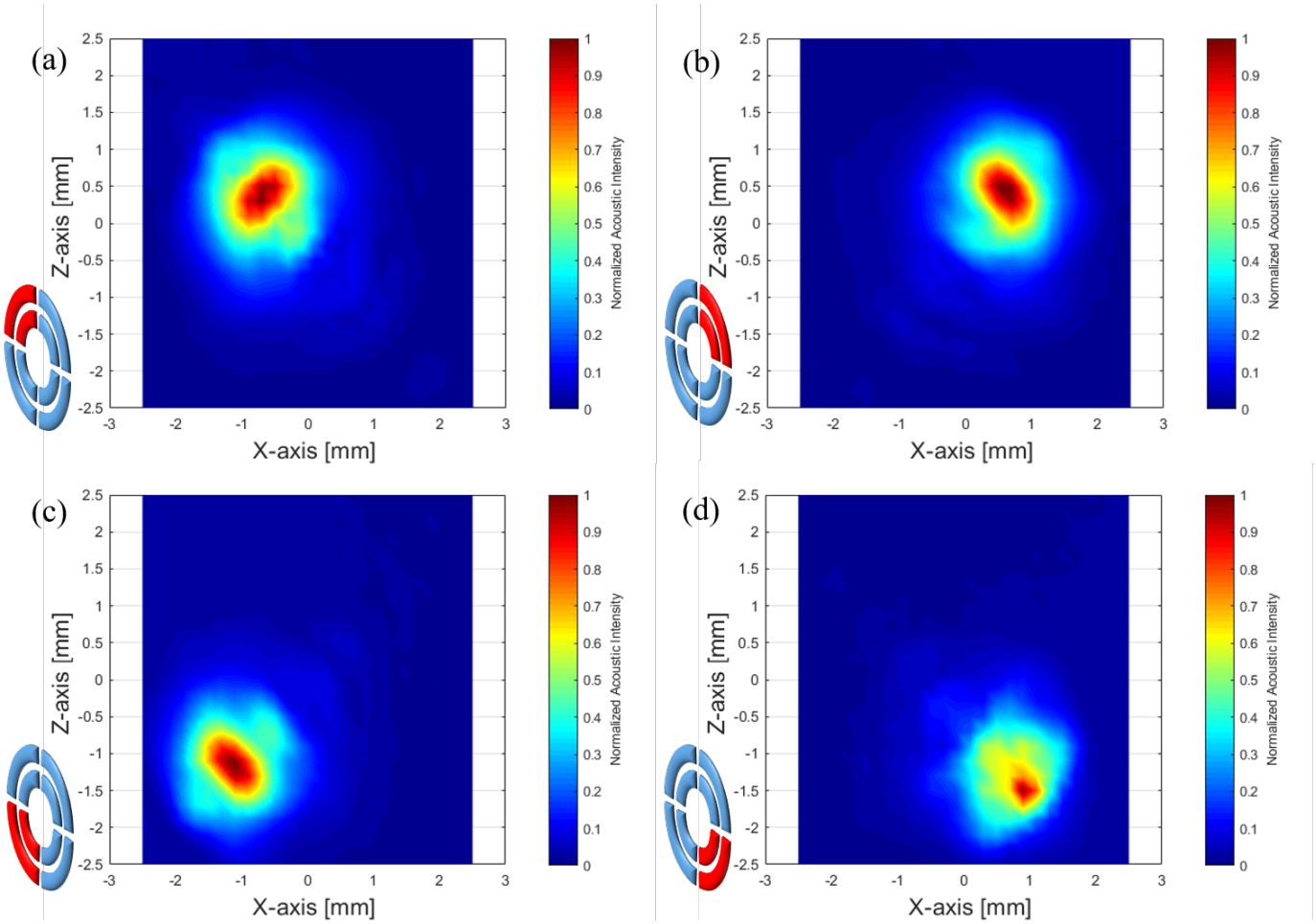

Fig. 14. The acoustic profile measurements for two electrodes at the same quarter in (a) top left, (b) top right, (c) bottom left, and (d) bottom right. It should be noted that in the schematic of the S-MRUT near each measurement, red shows the active electrodes and blue is for the inactive ones.

is $9.9059(\frac{mW}{mm^2})$. Note that, the FDA-allowed time-averaged acoustic intensity for body implants is $7.2(\frac{mW}{mm^2})$, although duty-cycling the signals based on the requirements allows us to provide stronger acoustic intensities. As shown in Fig. 15 the dust is capable of driving a μLED using the harvested ultrasonic power. It should also be noted that the video of this experiment is prepared as the supplementary information.

As an example of how the S-MRUT will work to selectively power the dusts, let us consider the schematic shown in Fig.16. In mice, the motor cortex starts from $0.5mm$ below the skull and the striatum is around $3mm$ below the skull. Given the focal distance of the S-MRUT from $1mm$ to $3mm$, it is able to transfer ultrasonic power to dusts in the cortex or on the surface of the striatum. To clarify the use of the proposed S-MRUT, an approach can be that two dusts separated by a distance (x) are placed on the surface of the striatum and in the cortex as shown in the Fig.16. Referring to our simulation and experimental results, each sector in a quarter of the S-MRUT has $0.862mm$ off-axis focal point on average. In other words, two dusts with maximum $1.725mm$ distance can be powered with two excited sectors in different quarters. Furthermore, another dust in depth of $1mm$ can be excited with the innermost sectors.

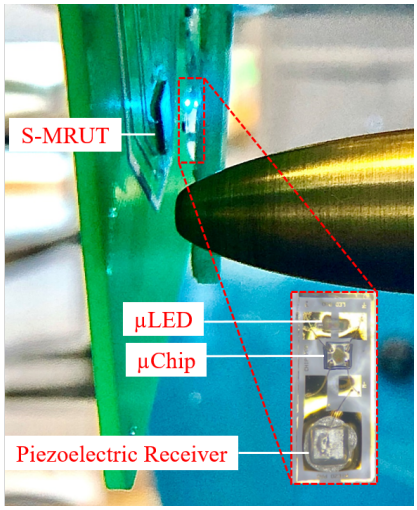

Fig. 15. Side view of the measurement setup. The hydrophone, the dust, and the S-MRUT are immersed in the water tank. μLED on the dust is lit up when the S-MRUT is delivering acoustic energy.

Since acoustic intensity will be attenuated by traveling through the brain tissue due to the absorption and reflection by the tissue, the S-MRUT is simulated when surrounded by brain

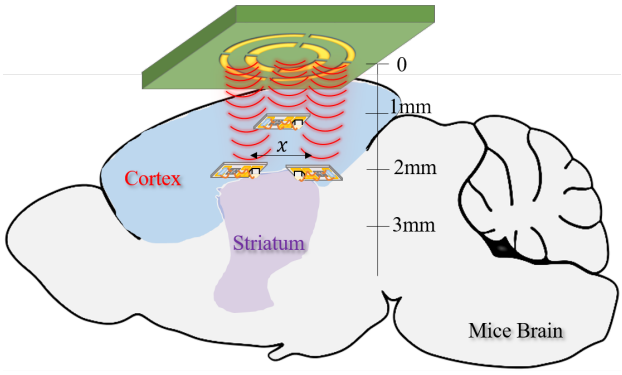

Fig. 16. Schematic of cross-section of mice brain with only motor cortex and striatum.

tissue and the results are compared with the water domain. Fig. 17 is given the result of the normalized acoustic intensity on the focal point for the inner excited rings. As shown in the figure the acoustic intensity is reduced by 15.7% through the brain tissue for the given frequency, which is as expected due to relatively short travel distance of ultrasonic waves through the mouse brain.

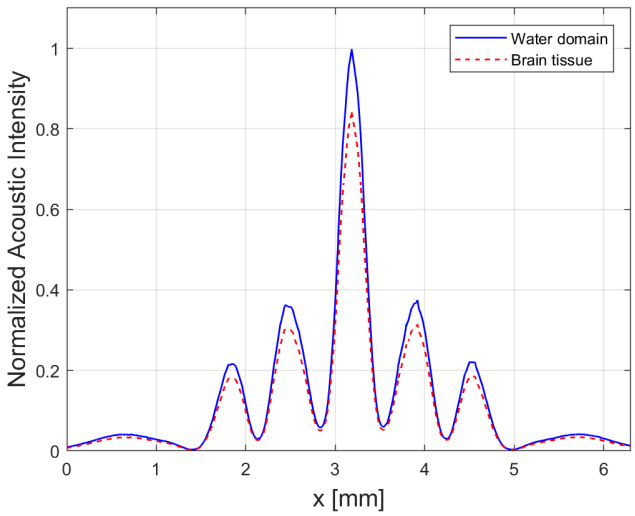

Fig. 17. Comparison of acoustic intensity on the focal plane into water domain and brain tissue.

V. Conclusion

In this paper, we presented a sectored multi ring ultrasonic transducer (S-MRUT) for powering mm-sized brain implants at different locations inside the brain using a single transducer, specifically designed for *in vivo* test in freely moving animals. With a goal of powering the dusts in the striatum of a mouse, the transducer was designed to sweep the focal point not only on the central axis in the range of $1-3mm$, but also in the lateral directions. To this end, the theories, design parameters, simulations, fabrication process, and experimental results for the proposed transducer were presented. In simulations, the resonance frequency for various cubic sizes of piezoelectric receivers with their resulting wavelength were investigated. Furthermore, the desired mode shape for the S-MRUT based on the resonance frequency was simulated. Moreover, the simulation and experimental results for acoustic profile of different configurations of the S-MRUT were presented. Based on simulation and experimental results, it was shown that the radius of steering area for the proposed transducer is equal to $0.678mm$ and $0.862mm$, respectively. Finally, the transducer was tested with our prepared dust in an experimental setup, and it showed the ability of powering the dust with a μLED for optical stimulation approach.

In future, the transducer will be tested for in-vivo experiments. In addition, the mechanical cross-coupling will be investigated for the S-MRUT.

Acknowledgment

This project (STARDUST) has received funding from the European Union's Horizon 2020 research and innovation program under grant agreement No 767092.

References

[1] M. A. Nicolelis, "Actions from thoughts," *Nature*, vol. 409, no. 6818, pp. 403–407, 2001.

[2] E. Dorsey, R. Constantinescu, J. Thompson, K. Biglan, R. Holloway, K. Kieburtz, F. Marshall, B. Ravina, G. Schifitto, A. Siderowf *et al.*, "Projected number of people with parkinson disease in the most populous nations, 2005 through 2030," *Neurology*, vol. 68, no. 5, pp. 384–386, 2007.

[3] A. Elkouzi, V. Vedam-Mai, R. S. Eisinger, and M. S. Okun, "Emerging therapies in parkinson disease—repurposed drugs and new approaches," *Nature Reviews Neurology*, vol. 15, no. 4, pp. 204–223, 2019.

[4] A. L. Benabid, S. Chabardes, J. Mitrofanis, and P. Pollak, "Deep brain stimulation of the subthalamic nucleus for the treatment of parkinson's disease," *The Lancet Neurology*, vol. 8, no. 1, pp. 67–81, 2009.

[5] H. Cagnan, T. Denison, C. McIntyre, and P. Brown, "Emerging technologies for improved deep brain stimulation," *Nature biotechnology*, vol. 37, no. 9, pp. 1024–1033, 2019.

[6] K. Deisseroth, "Optogenetics: 10 years of microbial opsins in neuroscience," *Nat. Neurosci*, vol. 18, no. 9, pp. 1213–1225, 2015.

[7] J. N. Stirman, M. M. Crane, S. J. Husson, S. Wabnig, C. Schultheis, A. Gottschalk, and H. Lu, "Real-time multimodal optical control of neurons and muscles in freely behaving caenorhabditis elegans," *Nature methods*, vol. 8, no. 2, p. 153, 2011.

[8] A. Rashidi, S. Hosseini, K. Laursen, and F. Moradi, "Stardust: Optogenetics, electrophysiology and pharmacology with an ultrasonically powered dust for parkinson's disease," in *2019 26th IEEE International Conference on Electronics, Circuits and Systems (ICECS)*. IEEE, 2019, pp. 109–110.

[9] A. S. Poon, S. O'Driscoll, and T. H. Meng, "Optimal frequency for wireless power transmission into dispersive tissue," *IEEE Transactions on Antennas and Propagation*, vol. 58, no. 5, pp. 1739–1750, 2010.

[10] H.-M. Lee, K. Y. Kwon, W. Li, and M. Ghovanloo, "A power-efficient switched-capacitor stimulating system for electrical/optical deep brain stimulation," *IEEE Journal of Solid-State Circuits*, vol. 50, no. 1, pp. 360–374, 2014.

[11] A. Rashidi, K. Laursen, S. Hosseini, H.-A. Huynh, and F. Moradi, "An implantable ultrasonically powered system for optogenetic stimulation with power-efficient active rectifier and charge-reuse capability," *IEEE Transactions on Biomedical Circuits and Systems*, vol. 13, no. 6, pp. 1362–1371, 2019.

[12] A. Rashidi, K. Laursen, S. Hosseini, and F. Moradi, "An ultrasonically powered optogenetic microstimulators with power-efficient active rectifier and charge reuse capability," in *2019 IEEE International Symposium on Circuits and Systems (ISCAS)*. IEEE, 2019, pp. 1–5.

[13] U. FDA, "Guidance for industry and fda staff information for manufacturers seeking marketing clearance of diagnostic ultrasound systems and transducers," *Rockville MD: FDA*, 2008.

[14] A. Arbabian, T. C. Chang, M. L. Wang, J. Charthad, S. Baltsavias, M. Fallahpour, and M. J. Weber, "Sound technologies, sound bodies: Medical implants with ultrasonic links," *IEEE Microwave Magazine*, vol. 17, no. 12, pp. 39–54, 2016.

[15] S. Hosseini, A. Rashidi, K. Laursen, J. Pelloux-Prayer, and F. Moradi, "Piezoelectric energy harvester with piezo-magnet stack for ultrasonically-powered brain implants," in *2019 IEEE International Ultrasonics Symposium (IUS)*. IEEE, 2019, pp. 201–204.

[16] K. Laursen, A. Rashidi, S. Hosseini, T. Mondal, B. Corbett, and F. Moradi, "Ultrasonically powered compact implantable dust for optogenetics," *IEEE Transactions on Biomedical Circuits and Systems*, pp. 1–1, 2020.

[17] D. Seo, J. M. Carmena, J. M. Rabaey, E. Alon, and M. M. Maharbiz, "Neural dust: An ultrasonic, low power solution for chronic brain-machine interfaces," *arXiv preprint arXiv:1307.2196*, 2013.

[18] A. Rashidi, K. Laursen, S. Hosseini, and F. Moradi, "Overvoltage protection circuits for ultrasonically powered implantable microsystems," in *2019 41st Annual International Conference of the IEEE Engineering in Medicine and Biology Society (EMBC)*. IEEE, 2019, pp. 4354–4358.

[19] T. Mondal, K. Laursen, S. Hosseini, A. Rashidi, F. Moradi, and B. Corbett, "Realization of high efficiency ultrasound-powered microleds for optogenetics," in *Integrated Photonics Platforms: Fundamental Research, Manufacturing and Applications*, vol. 11364. International Society for Optics and Photonics, 2020, p. 113641I.

[20] B. Herrera, F. Pop, C. Cassella, and M. Rinaldi, "Aln pmut-based ultrasonic power transfer links for implantable electronics," in *2019 20th International Conference on Solid-State Sensors, Actuators and Microsystems & Eurosensors XXXIII (TRANSDUCERS & EUROSENSORS XXXIII)*. IEEE, 2019, pp. 861–864.

[21] R. L. King, J. R. Brown, and K. B. Pauly, "Localization of ultrasound-induced in vivo neurostimulation in the mouse model," *Ultrasound in medicine & biology*, vol. 40, no. 7, pp. 1512–1522, 2014.

[22] E. F. Arkan and F. L. Degertekin, "Analysis and design of high-frequency 1-d cmut imaging arrays in noncollapsed mode," *IEEE transactions on ultrasonics, ferroelectrics, and frequency control*, vol. 66, no. 2, pp. 382–393, 2018.

[23] A. Halbach, P. Gijsenbergh, Y. Jeong, W. Devriese, H. Gao, M. Billen, G. B. Torri, C. Chare, D. Cheyns, X. Rottenberg *et al.*, "Display compatible pmut array for mid-air haptic feedback," in *2019 20th International Conference on Solid-State Sensors, Actuators and Microsystems & Eurosensors XXXIII (TRANSDUCERS & EUROSENSORS XXXIII)*. IEEE, 2019, pp. 158–161.

[24] J. Lee, K. Ko, H. Shin, S.-J. Oh, C. J. Lee, N. Chou, N. Choi, M. T. Oh, B. C. Lee, S. C. Jun *et al.*, "A mems ultrasound stimulation system for modulation of neural circuits with high spatial resolution in vitro," *Microsystems & nanoengineering*, vol. 5, no. 1, pp. 1–11, 2019.

[25] X. Jiang, H.-Y. Tang, Y. Lu, E. J. Ng, J. M. Tsai, B. E. Boser, and D. A. Horsley, "Ultrasonic fingerprint sensor with transmit beamforming based on a pmut array bonded to cmos circuitry," *IEEE transactions on ultrasonics, ferroelectrics, and frequency control*, vol. 64, no. 9, pp. 1401–1408, 2017.

[26] X. Jiang, Y. Lu, H.-Y. Tang, J. M. Tsai, E. J. Ng, M. J. Daneman, B. E. Boser, and D. A. Horsley, "Monolithic ultrasound fingerprint sensor," *Microsystems & nanoengineering*, vol. 3, no. 1, pp. 1–8, 2017.

[27] H. Kim, S. Kim, and H. J. Lee, "Capacitive micromachined ultrasonic transducer (cmut) ring array for transcranial ultrasound neuromodulation," in *2018 40th Annual International Conference of the IEEE Engineering in Medicine and Biology Society (EMBC)*. IEEE, 2018, pp. 2675–2678.

[28] G. Li, W. Qiu, Z. Zhang, Q. Jiang, M. Su, R. Cai, Y. Li, F. Cai, Z. Deng, D. Xu *et al.*, "Noninvasive ultrasonic neuromodulation in freely moving mice," *IEEE Transactions on Biomedical Engineering*, vol. 66, no. 1, pp. 217–224, 2018.

[29] C. Seok, Z. Ali, F. Y. Yamaner, M. Sahin, and Ö. Oralkan, "Towards an untethered ultrasound beamforming system for brain stimulation in behaving animals," in *2018 40th Annual International Conference of the IEEE Engineering in Medicine and Biology Society (EMBC)*. IEEE, 2018, pp. 1596–1599.

[30] S. Akhbari, F. Sammoura, and L. Lin, "Equivalent circuit models for large arrays of curved and flat piezoelectric micromachined ultrasonic transducers," *IEEE Trans. Ultrason., Ferroelectr, Freq. Control*, vol. 63, no. 3, pp. 432–447, 2016.

[31] S. Hosseini, K. Laursen, A. Rashidi, and F. Moradi, "Multi-ring ultrasonic transducer on a single piezoelectric disk for powering biomedical implants," in *2019 41st Annual International Conference of the IEEE Engineering in Medicine and Biology Society (EMBC)*. IEEE, 2019, pp. 3827–3830.

[32] D. Tarrazó-Serrano, S. Pérez-López, P. Candelas, A. Uris, and C. Rubio, "Acoustic focusing enhancement in fresnel zone plate lenses," *Scientific reports*, vol. 9, no. 1, pp. 1–10, 2019.

[33] D. Huang and E. Kim, "Micromachined acoustic-wave liquid ejector," *Journal of Microelectromechanical Systems*, vol. 10, no. 3, pp. 442–449, 2001.

[34] S. K. Edelman, *Understanding ultrasound physics*. Baker & Taylor, 2003.

[35] S.-C. Wooh and Y. Shi, "Optimum beam steering of linear phased arrays," *Wave motion*, vol. 29, no. 3, pp. 245–265, 1999.

[36] N. Kovačević, J. Henderson, E. Chan, N. Lifshitz, J. Bishop, A. Evans, R. Henkelman, and X. Chen, "A three-dimensional mri atlas of the mouse brain with estimates of the average and variability," *Cerebral cortex*, vol. 15, no. 5, pp. 639–645, 2005.

Seyedsina Hosseini received the B.Sc. degree in mechanical engineering from Azad University of Tehran, Iran in 2012. Due to his enthuthisasm in multidisciplinary fields, he pursued the master in Micro-and nanoelectromechanical Systems (MEMS&NEMS) engineering at University of Tehran, Iran and obtained his degree in 2016. He is currently with ICE-Lab, Aarhus University, as a Ph.D. fellow where he is working on MEMS-based piezoelectric ultrasonic transducers for brain implants powered by ultrasonic waves.

Kjeld Laursen received the B.Eng and M.Eng. degrees in electronics from Aarhus University, Denmark, in 2016 and 2019, respectively. He is currently pursuing a Ph.D. degree in electronics engineering with Integrated Circuit and Electronics Laboratory, Aarhus University. The focus of the Ph.D. studies are the design of ultra-low power integrated circuits for body implants. Before this, he used to work first as an electronic mechanic for BB Electronics A/S, Denmark, (2001 - 2006) including an apprenticeship. Later he studied as an electronic technician in Sønderborg, Denmark, (2006 - 2008), which led him to work in an R&D department for Siemens A/S Flow Instruments, Denmark, (2008 - 2012).

Amin Rashidi received the B.S. and M.S. degrees in electrical engineering both from K. N. Toosi University of Technology, Tehran, Iran, in 2011 and 2014, respectively. He was also with K. N. Toosi University of Technology, as a Laboratory Instructor and with the University of Allameh-Majlesi, Qazvin, Iran, as an Instructor from 2012 to 2014. From 2014 to 2017, he was with R&D department of Mega-Motor Company, Tehran, Iran, as an Electronic Systems Designer. Concurrently, he was also with the Research Laboratory for Integrated Circuits and Systems (ICAS) as an Associate Researcher at K. N. Toosi University of Technology. Currently, he is pursuing his studies in Integrated Circuit and Electronics Laboratory (ICE-LAB) at Aarhus University, Aarhus, Denmark, as a Ph.D. Fellow. His current research is focused on electronic circuits & systems design for implantable microsystems.

Tanmay Mondal received the B.Sc. degree in Physics from St. Xavier's College, Kolkata, India in 2012. He also completed his B.Tech. degree in Optics and Optoelectronics from University of Calcutta, India in 2015. Because of his enthusiasm for optics and optoelectronic fields, he pursued the master in Photonics at University of Eastern Finland, Finland and obtained his degree in 2017. He is presently pursuing his PhD in III-V materials and devices at Tyndall National Institute, Cork, Ireland. His present work is mainly focused on ultrahigh efficiency micro-LEDs for optogenetic applications. The work involves the design, fabrication, characterization of micro LEDs and their packaging for implantable microsystems.

Brian Corbett is head of the III–V Materials and Devices Group, Tyndall National Institute Cork, Ireland. He developed III–V devices and technology using dry and wet-etching techniques which been applied to InP, GaAs and GaN-based devices for low-cost single-frequency lasers, resonant cavity LEDs and photodetectors and micro-LEDs. He has co-authored over 200 papers. His current research interest is in the use of transfer printing to realise heterogeneous integration of III-V components for advanced photonic circuits.

Farshad Moradi (M'08, SM'18) received the BSc and MSc degrees electrical engineering from Isfahan University of Technology and Ferdowsi University of Mashhad, respectively. He received the PhD degree in electrical engineering from University of Oslo, Norway, in 2011. From 2009 to 2010, he visited the Nanoelectronic Laboratory, Purdue University, USA. He started his academic career as an assistant professor at the school of engineering at Aarhus university and currently an ssooiate professor with the department of engineering at Aarhus University. He is is the director of the Integrated Circuit and Electronics Laboratory (ICELab). He is reviewer of many Journals and has been served as technical committee of several conferences. He is an associate editor of Integration, the VLSI and VLSI Journal. He is the author/co-author of more than 80 Journal and Conference papers. His current research interests include ultra low-power integrated electronics from device to architecture.